

Rotorcraft Flowfield Prediction Accuracy and Efficiency using a Cartesian Grid Framework

Stephen M. Ruffin and Jae-Doo Lee

Abstract - Despite the high cost of memory and CPU time required to resolve the boundary layer, a viscous unstructured grid solver has many advantages over a structured grid solver such as the convenience in automated grid generation and shock or vortex capturing by solution adaption. In present study, an unstructured Cartesian grid solver is applied and results evaluated in rotorcraft flowfields. Recently, an existing solver, NASCART-GT was modified to use an immersed boundary approach (instead of a cut-cell approach). This approach is applied with ghost cell boundary condition, which increases the accuracy and minimizes unphysical fluctuations of the flow properties. The standard k-epsilon model by Launder and Spalding is employed for the turbulence modeling, and a new wall function was incorporated for the unstructured Cartesian grid solver. This model was previously only validated for 2-D flows, but in the present paper is applied to 3-D rotorcraft flowfields. For rotor modeling, an actuator disk model is chosen, since it is efficient and is widely verified in the study of the rotor-fuselage interaction. The full three dimensional calculations of Euler and RANS equations are performed for the GT rotor model and ROBIN configuration to test implemented actuator disk model along with the developed turbulence modeling.

Keywords – Cartesian Grid, Computational Fluid Dynamics, Rotorcraft, Turbulence Model

NOMENCLATURE

A	= blade area
A_0	= blade collective pitch angle
A_l	= lateral cyclic pitch angle
α_e	= effective angle of attack
α_i	= induced angle of attack
α_t	= twist angle at the blade tip
B_l	= longitudinal cyclic pitch angle
C_d	= sectional drag coefficient
C_l	= sectional lift coefficient
c	= chord length of rotor blade
D	= drag
Δ	= elemental value of blade
L	= lift
N	= number of blade
R	= rotor radius

T	= thrust
Θ	= pitch angle of blade
\mathbf{V}	= local velocity vector
$\boldsymbol{\Omega}$	= angular velocity vector

I. INTRODUCTION

THE interaction between the rotor and the helicopter fuselage generates complex flow field affecting vibration, acoustics and overall vehicle performance. If the performance of an isolated rotor and fuselage is analyzed separately, the interactional aerodynamics around the rotor-fuselage combination cannot be obtained by a simple linear superposition of each individual result because of the inherent nonlinear behavior of the flow. Therefore, the accurate prediction of rotor-fuselage interaction is essential for optimum design and analysis of rotorcraft.

To study the mutual effect of rotor and fuselage, the flow around a rotor must be modeled properly. Over the years, many rotor models have been developed to analyze rotor-fuselage interaction based on Euler or Navier-Stokes solver. Whitfield and Jameson [1] studied the propeller-wing interaction by introducing a source term in the Euler equation. Rajagopalan and Mathur [2] modeled the rotor as an actuator disk to solve incompressible Navier-Stoke equations around the rotor. The actuator disk is an infinitely thin disk, which carries discontinuities of flow properties using the source terms in the momentum and energy equations or enforcing the pressure jump on the disk boundary. The previous authors applied the source type actuator disk model, and Zori and Rajagopalan [3] employed this method to simulate the rotor-fuselage interaction. The boundary condition type actuator disk method has also been successfully used for many structured and unstructured solvers [4] – [7] for the rotor-fuselage interaction. Lately, O'Brien and Smith have published a series of papers [8]-[11] in which they discuss various computational techniques on the rotor-fuselage interaction including the actuator disk methods of boundary type and source type in an unstructured grid RANS solver. Hariharan and Sankar [12] and many other researchers utilize an overset grid method to solve the rotor-fuselage interaction phenomenon. They used the stationary frame around the fuselage and rotating frame near the rotor to capture the unsteady flow motion. Though the overset grid method gives detailed unsteady analysis, it is computationally expensive.

The CPU time and computer memory resources required for full three-dimensional, unsteady, viscous calculation of the rotating blade with the fuselage using unstructured grid solver are extreme. Use of such an approach for multiple

Manuscript received June 2, 2009.

S.M. Ruffin is with the School of Aerospace Engineering at the Georgia Institute of Technology, Atlanta, GA 30332-0150 USA. Phone: 404-894-8200; Fax: 404-894-2760; Email: Stephen.ruffin@ae.gatech.edu

J.D.Lee is with Samsung Heavy Industries, Co. LTD., Daejeon, 305-380, Korea

configurations considered in design or for a vehicle in maneuver is not practical. Meanwhile, the analysis using the actuator disk model, which has been widely verified in the analysis of the rotor-fuselage interaction is computationally less intensive than the full unsteady calculation, and may be suitable for some fuselage design and maneuver analysis. Two types of actuator disk formulations are common: boundary type and source type. Both approaches have been used very successfully for actuator disk modeling. In the present study, the boundary type actuator disk method is chosen, although both approaches are applicable to an unstructured Cartesian grid solver. Applying the boundary type actuator disk method in a Cartesian grid solver requires additional work in the grid generation. This is because the disk boundary should be aligned with the Cartesian cell faces, while the rotor location is independent of the grid in the source type method. However, the source type method is somewhat less robust and may give non-physical solution when the source spacing is coarser than the local grid spacing [9].

The first step in a CFD process is to choose an appropriate grid topology, which can be categorized into either structured or unstructured types depending on the data structure representing the grid points. In general, the fuselage configuration of a helicopter is complex and has many attachments. The flow field is also very complicated including vortex induced by the rotor and separation caused by bluff fuselage shape. An automated grid generation for complex fuselage and solution adaption for vortex capturing can be easily applied in an unstructured grid solver. In spite of the high cost of memory and CPU time inside the boundary layer, unstructured grid solvers have been very popular as high performance computers are recently available.

Relative to unstructured grid solvers using pyramid or prism type grid topology (see [13] and [14]), the numerical solution of the equations of fluid dynamics is simplified and the truncation error is reduced in a Cartesian-grid based methodology. When a cubic cell is generated in a Cartesian coordinate system, the computational domain should include arbitrary cut cell near the solid body [15]. A common problem with cut cell is the creation of very small cells, which lead to problems with stiffness of the equations, non-physical fluctuations of flow variables near the body, and very small time step [16]. Researchers have dealt with this in a number of ways, including hybrid grid topology [17], merged cut-cell method [18]-[20], embedded boundary method [21]-[22] and immersed boundary approach [26]-[31].

Since the hybrid grid topology employs structured grid near wall, laborious grid generation is required, while other approaches above are not. In the merged cut-cell and the embedded boundary methods, the centroids of boundary cells are not aligned with other flow cell centers as shown in Fig. 1. This limits the order of accuracy in spatial discretization. The immersed boundary approach has an advantage over other methods in the calculation of moving grid or geometry modification, since there is no need to modify boundary cell shape and its centroids. The details of these approaches are described by J. Lee [32].

The objective of present study is to demonstrate and evaluate use of a Cartesian grid methodology in turbulent

Navier-Stokes analysis or rotor-fuselage interaction problems. A wall function approach is employed to simulate turbulent flow around a rotorcraft effectively. Applying the wall function approach in an immersed Cartesian grid solver is very challenging, and has only been validated in 2-D studies [32]. In the present study, this approach is applied to 3-D rotorcraft applications. In order to model the rotor, the boundary condition type actuator disk approach is employed in the developed Cartesian grid solver. Unlike multiple overlapping structured grid topologies, the flow field around complex rotor-fuselage configurations can be modeled as a simple single block grid with unstructured meshes. The three-dimensional Euler calculation is performed over the GT rotor and the ROBIN configuration for the validation of the actuator disk model. The RANS calculation is performed over the GT rotor and the ROBIN rotorcraft model and compared with the Euler solution and experiments to test the capability of capturing viscous phenomena caused by the rotor-fuselage interaction.

II. NUMERICAL SOLVER

To provide for efficient, time-accurate solution of the Reynolds Averaged Navier-Stokes (RANS) equations, a dual time-stepping, multistage scheme has been employed. Hancock's two-stage scheme [33] has been used for time integration as used in compressible flow solver. It is known that the k - ϵ equations are instability prone during the transitory phase of the computations even with an implicit solver, when the leading part of the error surges out of the computational domain, generating large residuals. For stability, G.A. Gerolymos [34] used a limiter to bound k and ϵ in his implicit solver. Y. Zhao [35] introduced semi-implicit treatment of the source terms of k and ϵ equations. R.F. Kunz and B. Lakshminarayana [36] studied stability of explicit turbulent solvers. In NASCART-GT, the explicit time step is modified and the limiters of k and ϵ are used according to the stability analysis, in order to stabilize the computation and ensure the positivity of k and ϵ . Solution adaptation is performed based on divergence, vorticity and gradients of k and ϵ .

For proper calculation of high Reynolds number flow, the standard k - ϵ model by Launder and Spalding [37] is applied to

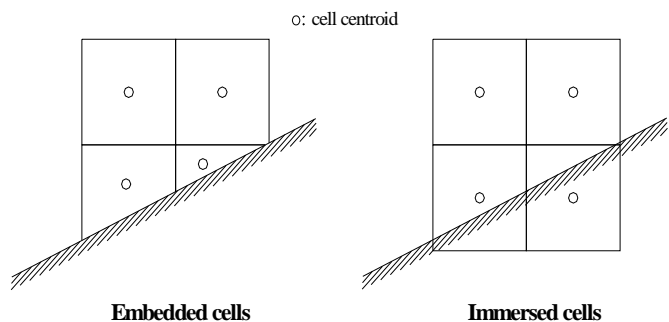


Fig. 1. Comparison of embedded and immersed cells.

the solver. To save the computer memory and CPU time in the calculation of turbulent boundary layer, a wall function approach is employed. In an immersed Cartesian grid system,

it is very difficult to apply the wall function approach. The traditional wall function approaches use either slip-wall or no-slip wall conditions, which requires smooth variation of grid cell distance from the wall to the flow cell center. The existence of cell centers located inside of the wall boundary has previously not been considered in such wall functions. However, the boundary cell centers in an immersed Cartesian grid are non-body-fitted so that certain cell centers are located inside of wall boundary and first. The traditional wall function methods are not applicable due to the problems of stability, accuracy and grid efficiency. The new wall function approach is based on the idea that the modified tangential velocity satisfying discrete wall shear stress approximation would eliminate the use of the complicated coordinate transformation. This makes the computational cells near wall to remain in numerically linear region, thereby, the computation would be stable. The new methodology is explained in detail by J. Lee [32].

III. ACTUATOR DISK MODEL

The rotor is modeled as a boundary type actuator disk with zero thickness, which represents an imaginary disk carrying pressure jump between the upper and lower surface allowing the flow to pass through. This approach reduces the computational resource requirement and eliminates the computational complexity of modeling each blade and performing time-accurate calculations. The simplest method to decide the pressure jump is applying predetermined pressure jump at the position of given radius. It restricts the variation of azimuthal variation of thrust. In current study, the pressure jump is specified using the blade element theory. It calculates the thrust from the intermediate flow variables during each iteration.

A. Fundamentals of Actuator Disk Model

The disk plane is represented by a finite number of rectangles, which exactly match one of the surfaces of hexahedral cells. The state vector at the cell center of a flow cell is calculated by integrating the fluxes on the six surfaces. Unlike the standard surface flux calculation, the state vector on the disk surface is specified by special treatment suggested by Fejtek and Roberts [4].

The points L and $L+1$ in Fig. 2 denote the upper and lower surfaces of a blade respectively and the main flow direction is aligned with negative z -axis. Consideration of the characteristics of the flow field indicates that for a subsonic inflow boundary, six flow properties must be specified and one can be extrapolated from the interior solution domain. The rotor grid point of disk surface L is considered to be an inflow boundary, such that four flow properties (i.e. ρ , u , v , p , k and \mathcal{E}) are specified from the outflow boundary condition and one property (i.e. w) is extrapolated from the inflow domain. The conditions at the interface are :

$$\rho_L = \rho_{L+1} \quad u_L = u_{L+1} \quad v_L = v_{L+1} \quad (\rho w)_L = (\rho w)_{L-1}$$

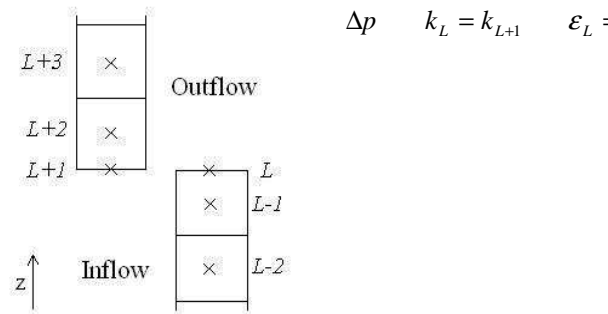


Fig. 2. Configuration of disk surface boundary condition.

The rotor grid point $L+1$ is regarded as an outflow boundary, where six flow properties are extrapolated and one (i.e. ρw) is fixed. The density ρ , the mass fluxes ρu and ρv , the total energy E_t , and mass fluxes of turbulent properties ρk and $\rho \mathcal{E}$ are updated using zero-order extrapolation from the solution domain at $L+2$. Mass continuity through the rotor disk is ensured by setting the z -directional mass flux to be conserved across the rotor disk.

$$\begin{aligned} \rho_{L+1} &= \rho_{L+2} & (\rho u)_{L+1} &= (\rho u)_{L+2} & (\rho v)_{L+1} &= (\rho v)_{L+2} \\ (\rho w)_{L+1} &= (\rho w)_L \\ (E_t)_{L+1} &= (E_t)_{L+2} & (\rho k)_{L+1} &= (\rho k)_{L+2} & (\rho \mathcal{E})_{L+1} &= (\rho \mathcal{E})_{L+2} \end{aligned} \quad (2)$$

In the current formulation, the tangential velocities normal to the rotor shaft are continuous across the rotor disk. Applying the torque boundary condition for the modeling of the rotor swirl described in [4] and [5] gives the tangential velocity jump. In the present work, the torque boundary condition is not considered, since effect is known to be small for the cases studied and it may lead to nonphysical solution [38]. The small effect of the torque boundary condition was shown by O'Brien and Smith [10], who computed GT rotor model using the actuator disk method. In the equations above, Δp represents the pressure jump across the rotor disk which generates the thrust of the rotor. The pressure jump is calculated using the blade element theory, which is described in the following.

B. Blade Element Theory (BET)

The blade element theory considers the variation of thrust in azimuth angle and cut-off radius. This approach is based on the 2-D airfoil theory, such that it neglects the 3-D wing tip effect of a blade. Even though the calculated pressure jump is nothing to do with the thrust coefficient at an intermediate stage, the final results should be converged to the given value. Configuration of a rotor blade is presented in Fig. 3.

The following description is from J. Lee and O.J. Kwon [39], and summarized for reader's convenience. V is continuous through the rotor disk plane, and its magnitude and direction are known as a part of the computation. Then, α_i at the center of each rectangular surface on the rotor disk, can be calculated as

$$\alpha_i = \text{Tan}^{-1}\left(\frac{V \cdot n}{V \cdot t}\right) \quad (3)$$

As shown in Fig. 3, the vector n denotes the unit vector normal to the rotor disk plane, and t unit vector tangential to the rotor disk plane. The tangential component of velocity vector includes contributions from the local flow velocity and the rotor rotational speed

$$V \cdot t = V \cdot p + (r \times \Omega) \cdot p \quad (4)$$

where p the unit vector parallel to the blade path. α_e is then

$$\alpha_e = \Theta - \alpha_i \quad (5)$$

In general, Θ is expressed as

$$\Theta = A_0 - A_1 \cos \psi - B_1 \sin \psi + \left(0.75 - \frac{r}{R}\right) \alpha_i \quad (6)$$

where ψ denote the blade twist angle at the tip. Since the velocity relative to the blade is known, elemental lift and drag acting at each section of the rotor blade can be calculated as

$$\Delta L = \frac{1}{2} \rho V_{rel}^2 C_l \Delta A \quad \Delta D = \frac{1}{2} \rho V_{rel}^2 C_d \Delta A \quad (7)$$

The velocity shown above is the relative velocity expressed as

$$V_{rel} = V + (r \times \Omega) \cdot p \quad (8)$$

The lift and drag coefficients are determined by using the 2-D airfoil theory. For N blades of the rotor, ΔT for each rectangle is scaled by a time factor, $N(d\psi/2\pi)$, to obtain time-averaged contribution while the rotor sweeps the azimuth angle of $d\psi$.

$$\Delta T = N \frac{d\psi}{2\pi} (\Delta L \cos \alpha_i - \Delta D \sin \alpha_i) \quad (9)$$

The time-averaged contribution above assumes that time for a blade sweeping a surface center is small relative to time for a round of a blade, i.e.

$$\frac{c}{r\Omega} \ll \frac{2\pi R}{R\Omega} \quad (10)$$

This assumption limits the ratio of chord length, c , to the radius of rotor disk surface, r .

$$\frac{c}{r} \ll 2\pi \quad (11)$$

Now, the azimuthal sweeping angle $d\psi$ can be replaced by the chord length and the radius of the rotor disk.

$$r d\psi \approx c \quad (12)$$

Substituting Eq. (12) into (9) gives the thrust expression for the present unstructured quadrangular surface mesh.

$$\Delta T = \frac{N\Delta A}{4\pi r} c \rho V_{rel}^2 (C_l \cos \alpha_i - C_d \sin \alpha_i) \quad (13)$$

The Prandtl-Glauert rule [40] is applied to include compressibility effect on the sectional lift and drag coefficient. Note that the thrust expression in Eq. (14) has a singular point at the rotor center. As the radius approaches to the center (i.e. $r \rightarrow 0$), the assumption in Eq. (11) does not hold anymore. The ratio of chord length to radius is, therefore, limited to 1/2.

$$\frac{c}{r} = \min\left(\frac{c}{r}, 0.5\right) \quad (14)$$

The difference in pressure between the upper and lower surface meshes of the rotor disk plane can be represented as

$$\Delta p = \frac{\Delta T}{\Delta A} \quad (15)$$

C. Rotor Trim

Rotor trim is added in the blade element method, and corrects collective and cyclic pitch angles in order to obtain the desired thrust and eliminate moments about the hub. Use

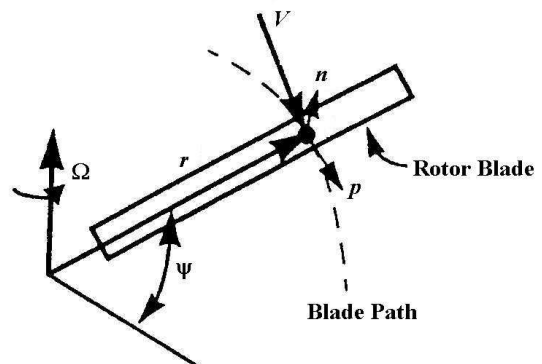


Fig. 3. Coordinate system of rotor blade from J. Lee and O.J. Kwon [39].

of the actual pitch angles (e.g. from an experimental model) generally results in errors in computed thrust and moment of the rotor. This is mainly due to the limitations of the actuator disk model. Since the time-averaged formulation and simplified lift and drag distributions of the blade element

method cannot properly simulate the unsteady flow over individual blade, the predicted thrust and moments are different from the measured values. The error is larger in the compressible flow solver than incompressible solver. In most compressible flow solver, the freestream Mach number is increased to avoid incompressible limit. The flow conditions around the actuator disk would be different due to the compressibility effects, although other nondimensional parameters are identical to the experiments. Therefore, the rotor trim routine is strongly required to properly compute the rotor-fuselage interaction.

The first step is to calculate the thrust coefficient and lateral and longitudinal moment coefficients about the hub are obtained by integrating the pressure jump on the actuator disk. Assuming simple linear relationships between the angles and coefficients, the new angles are found to get the desired thrust and zero moments. Then, calculate the coefficients again using the modified angles. This procedure is repeated until the angles are converged or a specified iteration number has been met.

IV. RESULTS

For the numerical investigation of rotor-fuselage interaction, two configurations are selected. The first is Georgia Tech (GT) rotorcraft model [41], which is geometrically simple and has been extensively studied. The second application is ROBIN airframe model that has been tested by Freeman and Mineck [42]. Both of the configurations are computed without rotor model first for validation of developed code. Then, the rotor model using actuator disk is tested.

A. GT Rotor Model

Fig. 4 shows the configuration of GT rotor model. The fuselage consists of hemisphere and cylinder body. Two rotor blades have a 2.7% cutout and rectangular planform of NACA0015 section. Each rotor blades are untwisted with a constant pitch angle of 10 degrees and zero cyclic pitch angle. The clearance between rotor and airframe, h/R , is 0.3. Since the fuselage length is not specified, it is assumed to three rotor radii. In the experiments, the fuselage is mounted on a strut, which is not modeled in the computation due to the lack of detail geometry. The freestream is parallel to the fuselage, and the rotor shaft is tilted 6 degrees. The measured flap angle is shown in Eq. (16) without pre-cone.

$$\beta = -2.02^\circ \sin \psi - 1.94^\circ \cos \psi \quad (16)$$

where β is a flap angle, and ψ an azimuth angle. The rotational speed of the rotor is 2100 RPM with an advance ratio of 0.1. The measured thrust coefficient, C_T , is 0.009045. The corresponding Reynolds number based on the fuselage length is 9.196×10^5 , and freestream Mach number 0.029, assuming standard atmosphere at sea level. In the computation, the freestream Mach number is increased to 0.3 to prevent instability caused by incompressibility, while other nondimensional parameters (i.e. Reynolds number, thrust coefficient, and advance ratio) are maintained.

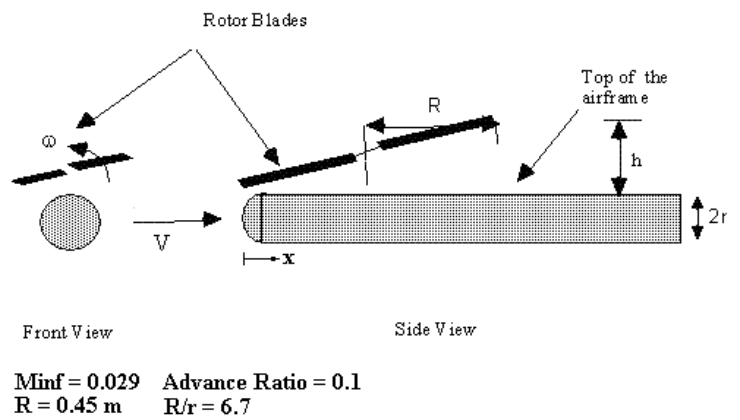


Fig. 4. Georgia Tech (GT) rotor.

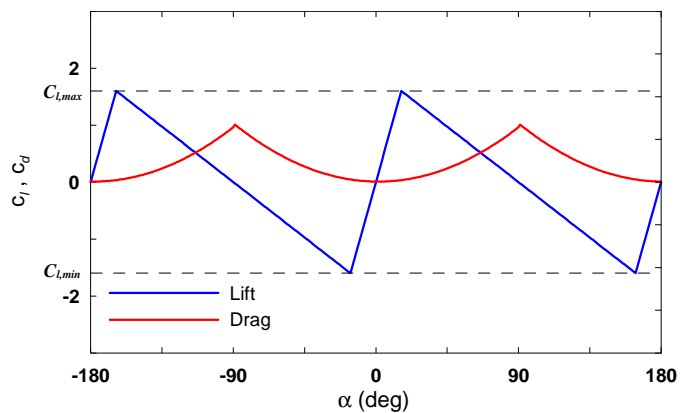


Fig. 5. Sectional lift and drag distributions in blade element method.

In the present study, three numerical cases are tested on the GT rotor model. First, the Euler and the RANS calculations are performed without accounting for a blade flapping motion, which is intended to investigate the viscous effect on the rotor-fuselage interaction. The other case considers the effect of the blade flapping in the RANS calculation. Two methods of the blade flap motion in the actuator disk method are known to date. One adds the flap velocity into the induced velocity normal to the disk plane that is located on the shaft plane [3], [43]. In the other method, the rotor disk is placed on the TPP without velocity modification [10]. In current study, the latter is chosen due to the difficulty in velocity scaling. A simple time derivative of the flap angle would not be suitable for specifying the disk boundary condition, since the freestream condition of the computation is different from the experiment. In addition, the flapping model using the TPP does not require an additional computation in the blade element method to find the flap velocity. In all three cases, the numerical boundaries are located 5 times of fuselage length from the center. The refinement level is 8 with a root cell dimension of $26 \times 22 \times 20$, which results in the largest y^+ of 169.9 and 218.6 for RANS calculations with and without flapping, respectively. The flow cells are refined at high gradient regions of divergence and vorticity. In the Euler calculation, the solution adaption is performed based only on the divergence. The total numbers of cells in the Euler and RANS calculations without flapping are 1,622,670 and 1,616,738, respectively, at the final iteration.

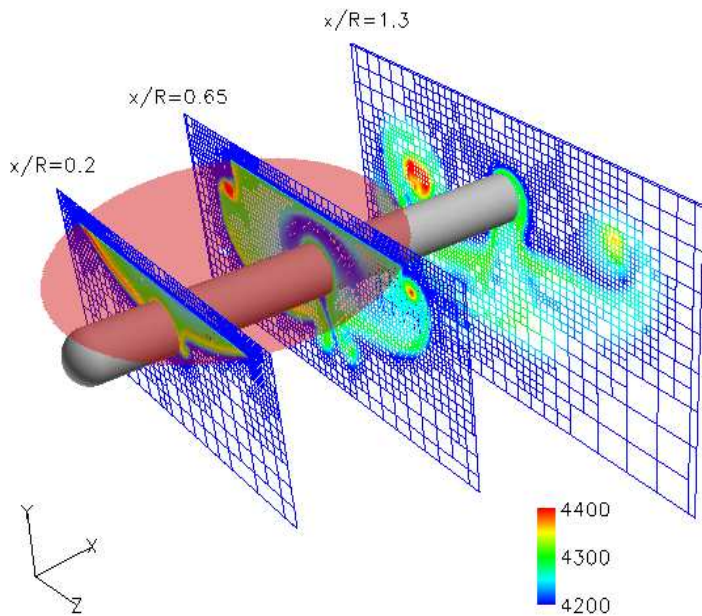


Fig. 6. Final grid configuration and entropy contours of GT rotor model from RANS calculation without flapping.

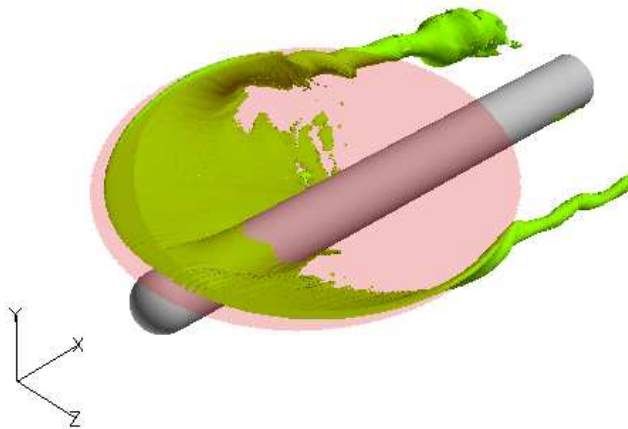


Fig. 7. Entropy iso-surfaces of GT rotor model from RANS calculation without flapping.

That of the RANS calculation with flapping is 1,599,970. The freestream turbulent intensity is assumed to be 1% and the normalized freestream eddy viscosity is 0.1. Assuming smooth wall on the rotor fuselage, the parameter related to the roughness parameter is set to 5.0 utilized in the law of the wall.

The rotor disks are located on the shaft plane in the Euler and RANS calculations. The sectional lift and drag applied in the blade element method are shown in Fig. 5. The maximal and minimal lift coefficients are assumed to be 1.6 and -1.6 at $\alpha = \pm 16^\circ$, which correspond to the airfoil data in [44]. The drag coefficient is obtained from the following equation.

$$c_d = 0.0087 - 0.0216\alpha + 0.4\alpha^2 \quad (17)$$

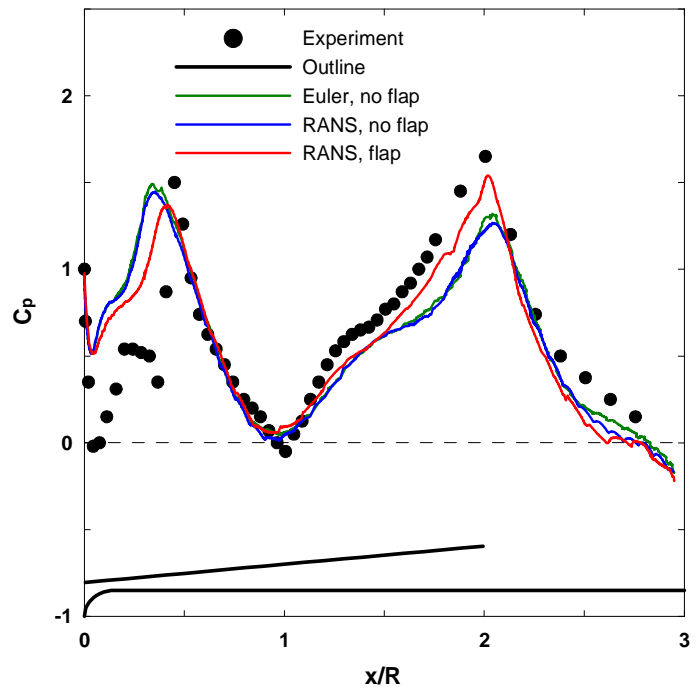


Fig. 8. Upper centerline pressure distribution for GT rotor model with rotor.

The constants used in the above equation are cited from Gessow and Tapscott [45]. The compressibility correction of the blade element method is not applied due to the low Mach number of the experimental model. The rotor trim analysis is performed at every 100 iterations to match the experimental rotor thrust. Since the GT rotor model has zero lateral and longitudinal cyclic pitch, only the collective pitch angle is adjusted by the trim loop.

The final grid configuration of a RANS calculation is shown with entropy contours in Fig. 6. The transparent red disk represents the actuator disk. Considering that the quantity of entropy is a measure of vorticity, the flow cells near the vortex core are automatically refined due to large vorticity. The cells near the rotor disk and the solid wall are also refined as a result of large divergence and vorticity, respectively. A close observation of the picture reveals that the vortex rollup generated at the tip of the rotor disk propagates and descends downstream. The tip vortex generated at the fore part of the disk propagates as a vortex sheet and dissipates rapidly, while the vortex generated at the lateral tips merges to a strong line vortex and travels further than the vortex sheet. This is clearly illustrated in Fig. 7, which shows iso-surfaces of the computed entropy. Note that the advancing side has a much stronger vortex rollup than the retreating side, since the rotor has a constant pitch angle.

The pressure distributions on the upper centerline of the GT rotor are shown in Fig. 8. The Euler and the RANS results without flapping are very close to each other, and clearly show the peaks and drop of the pressure caused by the rotor motion. The solution with flapping motion shows much better correlation with the experiment and better accuracy in the prediction of the peak pressure than the other solutions. Considering the fact that the current flap model does not require an additional computation, the accuracy can be easily

improved without extra cost. However, there still exists an inconsistency with the measured pressure near the nose and the local peak at $x/R = 0.3$. The predicted pressure near the fuselage tail is also lower than the experiment. Because many researchers (see [7], [10], and [39]) also found these flow patterns in their actuator disk modeling on the GT rotor, it

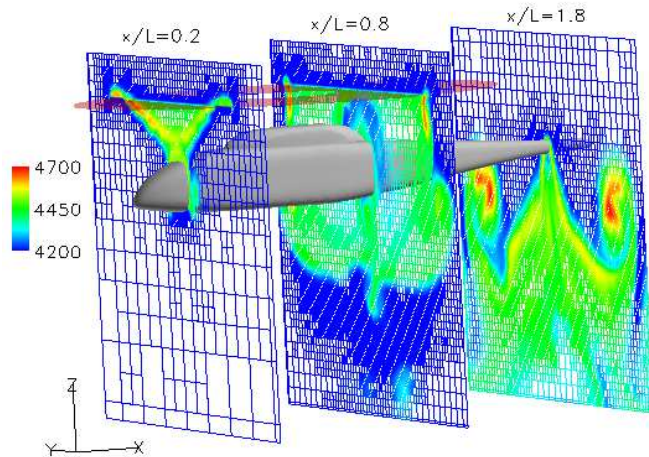


Fig. 9. Final grid and entropy contours of ROBIN.

seems that the discrepancies in the computed pressure are not due to a problem of the current solver, but a limit of the actuator disk model. As shown in the graph, the problems of the under-prediction of the peak pressures and their locations can be solved by adding the rotor flapping, but the local peak problem at $x/R = 0.3$ still remains. In the experiment, the local peak seems to be primarily caused by the unsteady wake effect of the rotor blade motion. An individual rotor blade generates a number of vortex filaments, which interact with the wakes from the other blades. Therefore, the resultant wake appears to form helical line vortex, not to be vortex sheet as shown in Fig. 7. A series of line vortices would be imposed on the surface, which drops the pressure. However, the actuator disk model is based on the time-averaged airfoil loading, which would not generate the helical shape line vortices but do the vortex sheet that dissipates rapidly. As explained above, the line vortex is stronger and propagates further than the vortex sheet. For more accurate calculation, a full unsteady computation might be required. This problem is analyzed and described well by O'Brien and Smith [10] who have extensively studied the rotor blade modeling. There is very small difference between the Euler and RANS results without flapping motion, excluding the fact that the RANS calculation results in slightly lower pressure due to the viscous dissipation and wake where the pressure peaks exist. This explains why other researchers (see [7] and [39]) employed an Euler solver to analyze the GT rotor configuration. The trimmed collective pitch angles are presented in Table 1, which are within 3% error from the test result.

B. ROBIN Rotorcraft Model

The Euler and RANS calculations using actuator disk are performed on the ROBIN (ROtor Body INteraction) model, which has been tested in NASA Langley in 2000 [46]. The fuselage shape is close to real helicopter, while its body is streamlined without any attachment for simplicity. The fuselage has the length of $2L$ where L represents the characteristic length. The fuselage centerline is yawed 1.2° nose left. The strut which supports the fuselage is mounted, is not modeled in the present study, since the detailed geometry is not known. The rotor consists of four blades, whose root cutout are at 24% of the radius, R , which is set to $R/L = 0.86$. The rotor blades have a rectangular planform with a chord of $0.066L$ and a linear twist of -8° . The center of the rotor hub is slightly offset to the advancing side, located at $x/L=0.696$, $y/L=0.051$, and $z/L=0.332$.

The computations are performed to match the test conditions of $\mu = 0.051$. Assuming standard air at sea level, the freestream Mach number and the Reynolds number based on the fuselage length are 0.0266 and 1.312×10^6 , respectively. The rotor shaft angle of attack is zero, and the measured thrust coefficient is 0.00636. The pitch angle of the rotor is given as

$$\theta = 5.9^\circ + 1.3^\circ \cos \psi - 1.3^\circ \sin \psi + 8^\circ \left(0.75 - \frac{r}{R} \right) \quad (18)$$

It is reported from the experiment that there is no significant pitch-flap coupling. Hence, the tip-path-plane is located normal to the rotor shaft and the coning angle is assumed to be zero. In both Euler and RANS calculations, the freestream Mach number is increased to 0.3, while the other nondimensional parameters are matching with the experiment.

The numerical boundaries are located 5 times of fuselage length from the center. The refinement level is 8 with a root cell dimension of $22 \times 16 \times 20$ to yield the maximum y^+ of 324.9 for RANS calculation. The Euler calculation also employs the same initial grid. The total numbers of cells in the final solutions are 740,377 and 1,614,516 for the Euler and the RANS calculations, respectively. The freestream turbulent intensity is assumed to be 1% and the normalized freestream eddy viscosity is 0.1. Assuming smooth wall on the rotor fuselage, the parameter related to the roughness parameter is set to 5.0 utilized in the law of the wall. The solution adaption is performed based on the divergence and vorticity as done in GT rotor calculation. The actuator disk is located on the rotor shaft plane. Since the airfoil section is not given, the lift and the drag in the blade element method follow the GT rotor case. The compressibility correction is not applied due to the low Mach number of the experimental model. The rotor trim analysis is performed at very 100 iterations to match the experimental rotor thrust and to eliminate the lateral and longitudinal moments about the hub.

Table 1. Trimmed collective pitch angles in GT rotor model.

	Experiment	Euler, no flap	RANS, no flap	RANS, flap
A_0 (degree)	10.0	9.879	9.856	9.720

The adapted grid configuration and entropy contours are shown in Fig. 9. As shown in the GT rotor case, strong line vortex is formed at lateral sides of the rotor disk and propagates downstream. The cells are refined along with the propagated wakes. Relatively low entropy region is shown at $x/L = 0.8$ in a doughnut shape, which is caused by the root cutout of the rotor. Since there is no blade loading inside the cutout region, the increase of the entropy is smaller than its surrounding.

The comparison of the computed pressure distribution on the upper centerline is presented in Fig. 10. The open symbols represent the steady state pressure, and the filled symbols represent the averaged value from unsteady pressure. Since the measured locations have slight offsets from the upper centerline, two values are plotted at the same x -locations. Both of the Euler and the RANS results are well correlated with the measured values, and there is not a large difference between them except the regions around the pylon and the nose. The difference between two numerical solutions occurred near the pylon is appears to be due to flow separation. The Euler solver can not simulate the flow separation. This produces the local pressure peak, which disappears in the RANS solution.

The sectional pressure distributions at various x -locations are shown in Fig. 11. The solutions from the Euler and the RANS calculations are similar and show good agreement with the experiment near the nose at $x/L = 0.353$. The difference between two solutions is increased as the sectional location approaches downstream. This seems reasonable since the boundary layer grows downstream and the difference between inviscid and viscous solution would be enlarged. However, the numerical solutions do not clearly distinguish the pressure on the lift and right surfaces and follow the measured value of one side at the tail region as shown in the picture d). One of the possible reasons is the difference of the model configurations between the computations and the experiment. In the wind tunnel test, there exist a rotor shaft above the pylon and a strut underneath the fuselage at $x/L \approx 1.0$, which is not reflected in the numerical analysis. These attachments would produce a complicated flow pattern that is different from the computational result. A close observation of Fig. 11 b) right aft of the strut reveals that the measured pressure is decreased at the bottom while the computed pressure is increased. In the experiment, the flow would separate around the strut and the resultant vortex would propagate downstream. This may affect the pressure field downstream and yield the discrepancy in Fig. 11 c). The rotor shaft is also likely to disturb the flow around the rotor disk, which alters the disk boundary condition and resultant disk loading. This may explain that the over-predicted pressure at the tail region in Fig. 11 and a large difference between numerically trimmed and measured pitch angles in Table 2.

V. CONCLUSIONS

In present study, new wall boundary conditions are implemented into the existing unstructured Cartesian grid framework. Instead of an embedded wall boundary, immersed boundary approach is applied with ghost cell boundary condition. The standard k -epsilon model by Launder and Spalding is employed in the calculation of RANS equations

for the turbulence modeling, and the RANS solver with developed boundary condition is applied in the analysis of the rotorcraft model with the actuator disk model to simulate the rotor-fuselage interaction. A number of conclusions are shown below.

- When the RANS solver with developed boundary condition is applied in the analysis of the rotorcraft model with the actuator disk model, the wakes created by the rotor disk are well captured using the adapted grid technique.
- The actuator disk model with the blade element method provides a good analysis of the steady state influence of the rotor in a couple in the computations of the GT rotor and the ROBIN model, although complicated unsteady effects may not be revealed. This yields a reasonable solution within the accuracy of the computational models used, and is computationally efficient (in terms of CPU time and memory on a single PC).
- The inclusion of blade flap into the actuator disk model improves the accuracy without an additional computation cost.
- Considering that the unstructured Cartesian grid solver has an advantage over the other grid topology in the grid generation over a complex geometry, the current research would provide a very useful aerodynamic tool in the preliminary design of a helicopter.

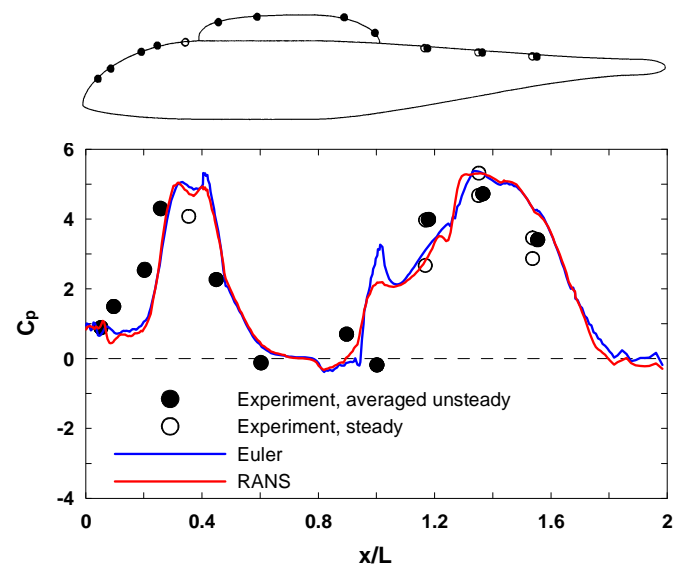


Fig. 10. Pressure distribution on the upper centerline of ROBIN configuration.

Table 2. Trimmed pitch angles of ROBIN model.

	Experiment	Euler	RANS
A_0 (degree)	5.9	10.12	10.05
A_1 (degree)	-1.3	-0.94	-0.98
B_1 (degree)	1.3	1.65	1.53

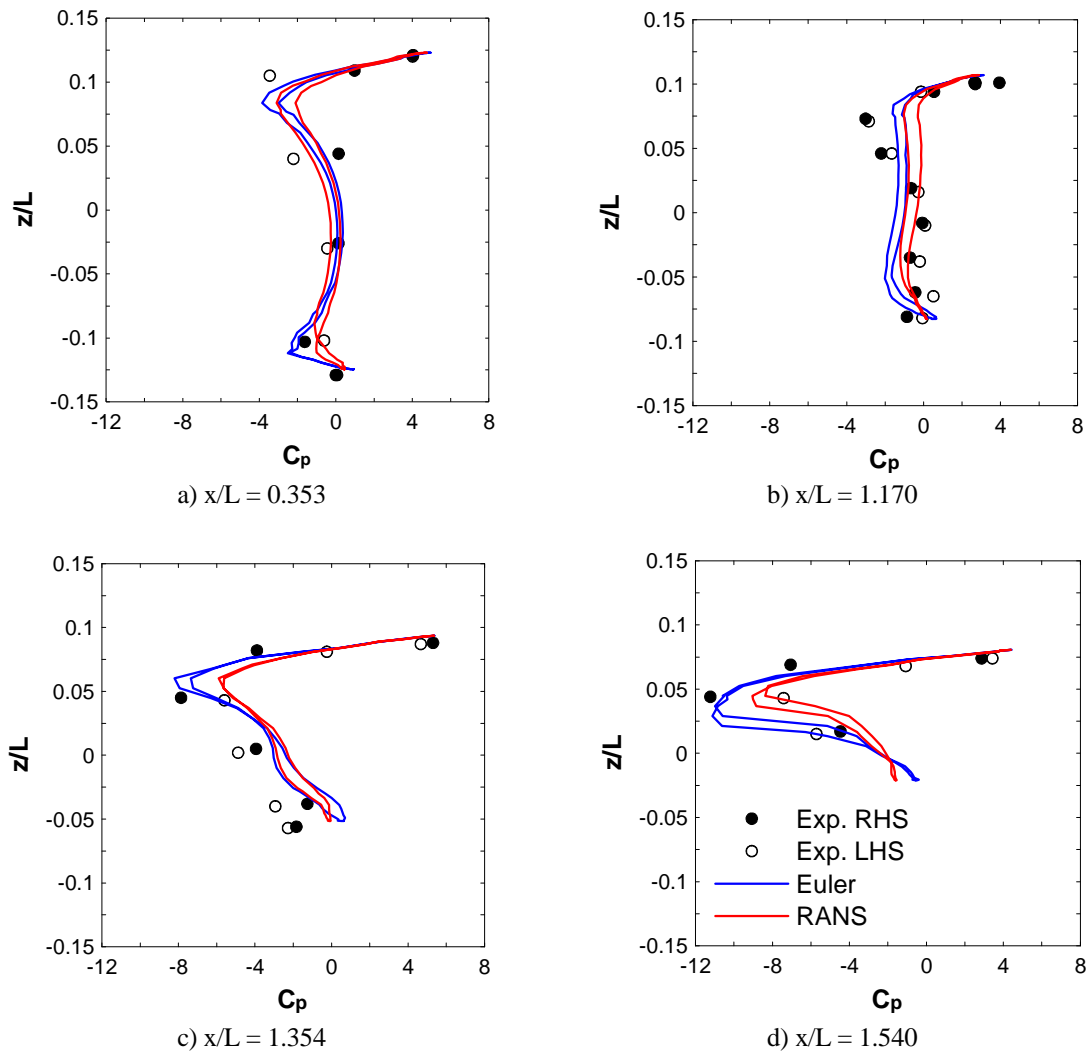


Fig. 11. Pressure distribution across ROBIN section.

REFERENCES

- [1] Whitfield, D. L., and Jameson, A., "Three Dimensional Euler Equation Simulation of Propeller-Wing Interaction in Transonic Flow," AIAA Paper 83-0236, 1983.
- [2] Rajagopalan, R. G., and Mathur, S. R., "Three-Dimensional Analysis of a Rotor in Forward Flight," *Journal of American Helicopter Society*, Vol. 38, 1993, pp. 14-25.
- [3] Zori, L. A., and Rajagopalan, R. G., "Navier-Stokes Calculations of Rotor-Airframe Interaction in Forward Flight," *Journal of American Helicopter Society*, Vol. 40, 1995, pp. 57-67.
- [4] Fejtek, I., and Roberts, L., "Navier-Stokes Computation of Wing/Rotor Interaction for a Tilt Rotor in Hover," *AIAA Journal*, Vol. 30, No. 11, 1992, pp. 2595-2603.
- [5] Chaffin, M. S., and Berry, J. D., "Helicopter Fuselage Aerodynamics Under a Rotor by Navier-Stokes Simulation," *Journal of American Helicopter Society*, Vol. 42, No. 3, 1997, pp. 235-242.
- [6] Bettschart, N., "Rotor Fuselage Interaction: Euler and Navier-Stokes Computations with an Actuator Disk," *55th Annual Forum of the American Helicopter Society*, Montreal, Canada, 1999.
- [7] Park, Y. M., Nam, H. J., and Kwon, O. J., "Simulation of Unsteady Rotor-Fuselage Interaction Using Unstructured Adaptive Meshes," *59th Annual Forum of the American Helicopter Society*, Phoenix, AZ, 2003.
- [8] O'Brien, D. M., and Smith, M. J., "Understanding the Physical Implications of Approximate Rotor Methods Using an Unstructured CFD Method," *31st European Rotorcraft Forum*, 2005.
- [9] O'Brien, D. M., and Smith, M. J., "Analysis of Rotor-Fuselage Interactions Using Various Rotor Models," AIAA Paper 2005-468, 2005.
- [10] O'Brien, D. M., and Smith, M. J., "Improvements in the Computational Modeling of Rotor/Fuselage Interactions Using Unstructured Grids," *61st Annual Forum of the American Helicopter Society*, Grapevine, TX, 2005.
- [11] Renaud, T., O'Brien, D., Smith, M., and Postdam, M., "Evaluation of Isolated Fuselage and Rotor-Fuselage Interaction Using CFD," *60th Annual Forum of the American Helicopter Society*, Baltimore, MD, 2004.
- [12] Hariharan, N., and Sankar, L., "Numerical Simulation of the Fuselage-Rotor Interaction Phenomenon," AIAA Paper 96-0672, 1996.
- [13] Koomullil, R.P., Soni, B.K., and Singh, R.K., "A Comprehensive Generalized Mesh System for CFD Applications," *Mathematics and Computers in Simulation*, Vol. 78, Issues 5-6, 2008, pp. 605-617.

- [14] Ito, Y., Shih, A. M., Erukala, A. K., Soni, B. K., Chernikov, A. N., Chrisochoides, N. P. and Nakahashi, K., "Parallel Mesh Generation Using an Advancing Front Method," *Mathematics and Computers in Simulation*, Vol. 75, Issues 5-6, 2007, pp. 200-209.
- [15] DM Ingram, DM Causon and CG Mingham, "Developments in Cartesian Cut Cell Methods", *Mathematics and Computers in Simulation* 61(3-6), 2003, 561-572.
- [16] Marshall, D. D., "Extending the Functionalities of Cartesian Grid Solvers: Viscous Effects Modeling and MPI Parallelization," Ph.D. Thesis, Georgia Institute of Technology, Atlanta, GA, 2002.
- [17] Charlton, E. F., "An Octree Solution to Conservation-laws over Arbitrary Regions (OSCAR) with Applications to Aircraft Aerodynamics," Ph.D. Thesis, University of Michigan, Ann Arbor, MI, 1997.
- [18] Udaykumar, H. S., Mittal, R., Rampunggoon, P., and Khanna, A., "A Sharp Interface Cartesian Grid Method for Simulating Flows with Complex Moving Boundaries," *Journal of Computational Physics*, Vol. 174, 2001, pp. 345-380.
- [19] Udaykumar, H. S., Kan, H., Shyy, H., and Tran-son-tay, R., "Multiphase Dynamics in Arbitrary Geometries on Fixed Cartesian Grids," *Journal of Computational Physics*, Vol. 137, No. 2, 1997, pp. 366-405.
- [20] Ye, T., Mittal, R., Udaykumar, H. S., and Shyy, W., "An Accurate Cartesian Grid Method for Viscous Incompressible Flows with Complex Immersed Boundaries," *Journal of Computational Physics*, Vol. 156, 1999, pp. 209-240.
- [21] Marshall, D., and Ruffin, S., "A New Inviscid Wall Boundary Condition Treatment for Embedded Boundary Cartesian Grid Schemes," AIAA Paper 2004-583, 2004.
- [22] Marshall, D., and Ruffin, S., "An Embedded Boundary Cartesian Grid Scheme for Viscous Flows Using a New Viscous Wall Boundary Condition Treatment," AIAA Paper 2004-581, 2004.
- [23] Berger, M. J., and Leveque, R. J., "Stable Boundary Conditions for Cartesian Grid Calculations," NASA CR-182048, 1990.
- [24] Aftosmis, M. J., Berger, M. J., and G. Adomavicius, "A Parallel Multilevel Method for Adaptively Refined Cartesian Grids with Embedded Boundaries," AIAA Paper 2000-0808, 2000.
- [25] Murman, S. M., Aftosmis, M. J., and Berger, M. J., "Implicit Approaches for Moving Boundaries in a 3-D Cartesian Method," AIAA Paper 2003-1119, 2003.
- [26] Forrer, H., and Jeltsch, R., "A Higher-Order Boundary Treatment for Cartesian-Grid Method," *Journal of Computational Physics*, Vol. 140, 1998, pp. 259-277.
- [27] Dadone, A., and Grossman, B., "Rapid Aerodynamic Optimization Using Far-Field Coarsened Cartesian Grids," AIAA Paper 2004-4477, 2004.
- [28] Dadone, A., and Grossman, B., "Far-Field Coarsening and Mesh Adaptation for Inviscid Flows on Cartesian Grids," AIAA Paper 2004-0585, 2004.
- [29] Dadone, A., and Grossman, B., "Further Developments in the Three-Dimensional Cartesian-Grid Ghost-Cell Method," AIAA Paper 2006-1085, 2006.
- [30] Dadone, A., and Grossman, B., "Ghost-Cell Method for Inviscid Three-Dimensional Flows on Cartesian Grids," AIAA Paper 2005-874, 2005.
- [31] Dadone, A., and Grossman, B., "An immersed body methodology for inviscid flows on Cartesian grids," AIAA Paper 2002-1059, 2002.
- [32] Lee, J., "Development of an Efficient Viscous Approach in a Cartesian Grid Framework and Application to Rotor-Fuselage Interaction," Ph.D. thesis, Georgia Institute of Technology, Atlanta, GA, 2006.
- [33] Tu, S., "Development of a Solution Adaptive Cartesian-Grid Solver for 2-D Thermochemical Nonequilibrium Flows," Ph.D. Thesis, Georgia Institute of Technology, Atlanta, GA, 2001.
- [34] Gerolymos, G. A., "Implicit Multiple-Grid Solution of the Compressible Navier-Stokes Equations Using k- ϵ Turbulence Closure," *AIAA Journal*, Vol. 28, No. 10, 1990, pp. 1707-1717.
- [35] Zhao, Y., "Stable Computation of Turbulent Flows with a Low-Reynolds-Number k- ϵ Turbulence model and Explicit Solver," *Advances in Engineering Software*, Vol. 28, 1997, pp. 487-499.
- [36] Kunz, R. F., and Lakshminarayana, B., "Stability of Explicit Navier-Stokes Procedures Using k- ϵ and k- ϵ /Algebraic Reynolds Stress Turbulence Models," *Journal of Computational Physics*, Vol. 103, 1992, pp. 141-159.
- [37] Launder, B. E., and Spalding, D. B., "The Numerical Computation of Turbulent Flows," *Computer Methods in Applied Mechanics and Engineering*, Vol. 3, 1974, pp. 269-289.
- [38] Chaffin, M. S., and Berry, J. D., "Navier-Stokes Simulation of a Rotor Using a Distributed Pressure Disk Method," *51st Annual Forum of the American Helicopter Society*, Fort Worth, TX, 1995.
- [39] Lee, J., and Kwon, O. J., "Predicting Aerodynamic Rotor-Fuselage Interactions by Using Unstructured Meshes," *Transactions of The Japan Society for Aeronautical and Space Sciences*, Vol. 44, No. 146, 2002, pp. 208-216.
- [40] Anderson, J. D., *Modern Compressible Flow with Historical Perspective*, 2nd ed., McGraw-Hill, 1990.
- [41] Brand, A. G., "An Experimental Investigation of the Interaction Between a Model Rotor and Airframe in Forward Flight," Ph.D. Thesis, Georgia Institute of Technology, Atlanta, 1989.
- [42] Freeman, C. E., and Mineck, R. E., "Fuselage Surface Pressure Measurements of a Helicopter Wind-Tunnel Model with a 3.15-Meter Diameter Single Rotor," NASA TM 80051, 1979.
- [43] Zori, L. A., Mathur, S. R., and Rajagopalan, R. G., "Three-Dimensional Calculations of Rotor-Airframe Interaction in Forward Flight," *48th Annual Forum of the American Helicopter Society*, Washington, D.C., 1992.
- [44] Abbott, I. H., and Von Doenhoff, A. E., *Theory of Wing Sections*, Dover ed., 1959.
- [45] Gessow, A., and Tapscott, R. J., "Charts for Estimating Performance of High-Performance Helicopters," NACA Report 1266, 1956.
- [46] Mineck, R. E., and Gorton, S. A., "Steady and Periodic Pressure Measurements on a Generic Helicopter Fuselage Model in the Presence of a Rotor," NASA TM-2000-210286, 2000.